

# UltraGS: Gaussian Splatting for Ultrasound Novel View Synthesis

Yuezhe Yang, Wenjie Cai, Dexin Yang, Yufang Dong, Xingbo Dong, Zhe Jin

Anhui Provincial International Joint Research Center for Advanced Technology in Medical Imaging,  
Anhui University

## Abstract

*Ultrasound imaging is a cornerstone of non-invasive clinical diagnostics, yet its limited field of view complicates novel view synthesis. We propose **UltraGS**, a Gaussian Splatting framework optimized for ultrasound imaging. First, we introduce a depth-aware Gaussian splatting strategy, where each Gaussian is assigned a learnable field of view, enabling accurate depth prediction and precise structural representation. Second, we design **SH-DARS**, a lightweight rendering function combining low-order spherical harmonics with ultrasound-specific wave physics, including depth attenuation, reflection, and scattering, to model tissue intensity accurately. Third, we contribute the **Clinical Ultrasound Examination Dataset**, a benchmark capturing diverse anatomical scans under real-world clinical protocols. Extensive experiments on three datasets demonstrate UltraGS’s superiority, achieving state-of-the-art results in PSNR (up to 29.55), SSIM (up to 0.89), and MSE (as low as 0.002) while enabling real-time synthesis at 64.69 fps. The code and dataset are open-sourced at: <https://github.com/Bean-Young/UltraGS>.*

## 1. Introduction

Ultrasound imaging is highly valued for its non-invasive nature, real-time capabilities, and cost-effectiveness [37]. Despite these advantages, obtaining a complete field of view during ultrasound examinations remains challenging due to its inherently limited scanning angle [1]. This limitation complicates the integration of two-dimensional ultrasound images into reliable 3D models, a critical process for precise diagnosis and treatment planning. Moreover, ultrasound data exhibits anisotropic characteristics, leading to inconsistencies that adversely affect the accuracy of novel view synthesis [12]. Traditional approaches, such as swinging probes [2] and 2D transducer arrays [16], have been developed to address these challenges. However, these methods depend heavily on manual alignment, increasing susceptibility to errors, and are typically expensive and impractical

for widespread clinical adoption [29].

Computer-assisted approaches offer a potential solution by enabling the generation of precise and consistent 3D representations from 2D ultrasound scans, thereby enhancing the completeness of ultrasound imaging views [34]. Early methods, such as computational and sensorless 3D ultrasound, were developed to reduce costs and improve imaging quality [20]. However, these approaches often struggled to accurately model anatomical structures, resulting in artifacts and inconsistencies. More recently, deep learning techniques have been integrated into ultrasound imaging, utilizing data-driven methods to learn imaging patterns and improve the quality of synthesized novel ultrasound views [10, 26]. Despite these advancements, existing explicit reconstruction methods remain limited in their capacity to model complex anatomical structures and fail to generate consistent B-mode ultrasound images from arbitrary viewpoints [28]. Additionally, the data-driven nature of deep learning introduces challenges related to privacy protection [23] and domain shift [17].

Recently, NeRF, an implicit unsupervised learning method [27], has shown promise in ultrasound’s novel view synthesis. It learns a continuous 3D scene from sparse multi-view images, enabling high-quality, consistent image synthesis without stitching errors [27]. Ultra-NeRF enhances this by integrating ultrasound physics, producing accurate and physically consistent B-mode ultrasound images [36].

However, NeRF relies on volume ray marching through an MLP for novel view synthesis [3]. This requires sampling a large number of 3D points per ray, making it computationally expensive [7]. For real-time medical imaging, this high computational demand is a critical limitation. In 2023, 3D Gaussian Splatting (3DGS) was introduced as a solution to NeRF’s inefficiency [24]. By using explicit Gaussians, 3DGS enables real-time rendering while preserving fine details and adapting to viewpoint changes. In medical imaging, 3DGS has already been explored for X-ray CT reconstruction [7, 14]. Nevertheless, direct application to ultrasound imaging is not straightforward due to fundamental differences among B-mode ultrasound, natural images, and

X-rays. Standard 3DGS represents a scene as a collection of Gaussian primitives and synthesizes new views by projecting and accumulating their contributions. X-Gaussian further adapts this formulation by replacing color with a transmission–attenuation model, which is consistent with the physics of X-ray imaging. Ultrasound, however, is not a transmission-based modality but instead relies on complex wave propagation phenomena, including scattering, reflection, and attenuation. Thus, simple Gaussian accumulation based on transmission cannot accurately describe its physical process.

The primary challenge of applying 3DGS to ultrasound imaging lies in the lack of depth information suited for tissue structures. In natural images, implicit depth encoded in the Gaussian point positions is often sufficient [6]. In contrast, ultrasound requires explicit modeling of tissue surfaces and the interaction between acoustic waves and these surfaces to recover realistic structural depth [8].

Another key challenge arises from the fundamental difference in field-of-view (FoV). While in natural imaging the FoV is fixed by the camera lens, in ultrasound the effective FoV can vary even within a single scan due to depth-dependent imaging ranges, dynamic beam focusing, and probe motion. This dynamic FoV variability introduces additional complexity for ultrasound-specific 3DGS.

A further difficulty lies in modeling ultrasound intensity. Although ultrasound shares anisotropic effects with natural images, it is far more influenced by nonlinear processes such as depth-dependent attenuation, reflection, and scattering. Direct physical simulation of these wave interactions is computationally prohibitive. Therefore, lightweight and differentiable approximations of these physical processes must be designed to capture the essential visual characteristics while remaining compatible with gradient-based optimization frameworks.

To address these challenges, we propose UltraGS, a real-time depth-aware 3D Gaussian Splatting framework tailored for B-mode ultrasound imaging. UltraGS enables depth-aware rendering by introducing learnable fields of view for each Gaussian point and incorporates ultrasound wave propagation properties to achieve accurate and efficient novel-view synthesis.

Our key contributions are as follows:

- We present the first adaptation of 3DGS to medical ultrasound imaging, explicitly incorporating its unique acoustic properties and filling a critical gap in the field.
- Technically, we design a depth-aware Gaussian splatting strategy that transforms between 3D spatial points and 2D surface points, while assigning each Gaussian a learnable field of view for precise structural representation. We further develop the SH-DARS rendering function, which combines low-order spherical harmonics with essential ultrasound propagation effects

(depth attenuation, reflection, scattering) to faithfully reproduce tissue intensities.

- We introduce the Clinical Ultrasound Examination Dataset, a publicly available benchmark collected under real clinical protocols.
- We conduct extensive evaluations on three distinct datasets, achieving state-of-the-art results across multiple metrics (PSNR up to 29.55, SSIM up to 0.89), while maintaining a real-time rendering speed of 64.69 fps.

## 2. Related Work

### 2.1. Novel View Synthesis (NVS)

Significant progress in novel view synthesis (NVS) has been achieved with the advent of NeRF [27]. NeRF employs a multi-layer perceptron (MLP) to implicitly model scene geometry and appearance, optimized through volume rendering, thereby achieving remarkable rendering quality. Subsequent works, such as Mip-NeRF and its variants [4, 5, 21], have addressed aliasing artifacts inherent in NeRF-based approaches. Additionally, improvements in rendering efficiency have been realized via distillation techniques [30, 39] and baking strategies [11, 31]. Nevertheless, despite substantial gains in visual fidelity, NeRF remains computationally intensive due to its implicit representation and the high cost of volume ray marching [41], making real-time performance difficult to achieve.

Recently, 3D Gaussian Splatting (3DGS) [24] has emerged as a promising approach for real-time rendering by explicitly representing scenes with millions of learnable Gaussian points. Leveraging its explicit representation and a rasterization-based pipeline, 3DGS achieves significant efficiency gains. This explicit framework has been further enhanced by SuGaR [18], which aligns Gaussians to scene surfaces for rapid and high-quality mesh extraction, and by Mip-Splatting [40], which introduces frequency-aware smoothing and Mip-level filtering to suppress aliasing artifacts and improve robustness under varying sampling conditions. Kumar et al. [25] proposed a depth-aware 3D Gaussian splatting approach for few-shot novel view synthesis, incorporating monocular depth prediction as a prior and employing a scale-invariant depth loss to constrain 3D geometry. Their method models color using low-order spherical harmonics to avoid overfitting while retaining all splatted points rather than periodically discarding low-opacity points.

Although 3DGS has advanced rapidly in recent years, its ability to synthesize novel views in medical ultrasound imaging remains limited. Methods designed for natural scenes fail to account for the unique properties of ultrasound and its depth imaging principles. To bridge this gap, our work integrates ultrasound propagation properties into

the 3DGS framework, constructing depth-aware Gaussian spheres to enable effective novel view synthesis for ultrasound imaging.

## 2.2. NVS in Medical Imaging

Accurate 3D representations in medical imaging can greatly enhance reconstruction precision and efficiency, thereby enabling effective novel view synthesis (NVS). In the field of ultrasound imaging, NVS methods such as Ultra-NeRF [12] have incorporated ultrasound-specific physical modeling and diffusion-based generative priors. By explicitly adapting NeRF frameworks to ultrasound, these approaches improve the fidelity of synthesized views.

With the advancement of 3DGS, Gaussian-based representations for NVS have also achieved significant progress in medical imaging [38]. For instance, X-Gaussian [7] and DDGS-CT [15] were among the first to apply 3DGS to NVS in X-ray and CT imaging. X-Gaussian eliminated view dependency and introduced an optimized initialization strategy that substantially improved the synthesis of novel CT views. DDGS-CT further enhanced reconstruction accuracy by adopting a radiodensity-aware sampling strategy, outperforming previous NVS methods across various quantitative metrics and clinical applications.

However, despite the success of these 3DGS-based NVS methods in CT imaging, their direct application to ultrasound remains challenging. The unique characteristics of ultrasound, including anisotropic wave propagation, depth-dependent attenuation, and scattering, introduce new complexities for Gaussian-based representations. To address these challenges, we propose a depth-aware Gaussian rendering method specifically designed for ultrasound, aiming to more accurately model its 3D structure and enable reliable novel view synthesis.

## 3. Methods

Our UltraGS pipeline (Fig.1) introduces two key innovations for ultrasound-specific novel view synthesis: **(1)** A depth-aware Gaussian splatting method that adapts to ultrasound imaging characteristics (Fig.1a), and **(2)** SH-DARS, a differentiable rendering function combining depth attenuation, reflection, and scattering effects with low-order spherical harmonics (Fig.1b). This framework enables accurate Gaussian representations from sparse viewpoints, supporting novel view synthesis through physics-informed intensity rendering.

### 3.1. Preliminaries of Gaussian Splatting

In 3DGS [24], the initial Gaussian model takes a sparse point cloud obtained from Structure-from-Motion (SfM) camera calibration as input. Each 3D Gaussian in the scene is defined by its position  $\mu$  and covariance matrix  $\Sigma$ . During rendering, to project the 3D Gaussians onto a 2D plane,

the world-space covariance matrix is transformed into the camera-space using the method proposed by Zwicker et al. [42, 43]:

$$\Sigma' = JW\Sigma W^\top J^\top, \quad (1)$$

where  $J$  is the Jacobian of the affine approximation of the projective transformation, and  $W$  is a viewing transformation matrix.

The reliance of 3DGS on viewpoint parameters, often absent in clinical ultrasound, leads to geometric inconsistencies, as the projected Gaussian shapes vary across different views, causing rendering artifacts (Fig. 2(a)). The absence of fixed normal directions in 3D Gaussians introduces depth map offsets (Fig. 2(b)), which are critical for clinical diagnosis. While improvements in depth rendering have been proposed, misalignment issues persist. Our model overcomes these limitations, achieving superior consistency and accuracy compared to 3DGS (Fig. 2).

### 3.2. Depth-aware Gaussian Splatting

Unlike traditional 3DGS, we have designed a depth-aware Gaussian splat that addresses the unique challenges of ultrasound imaging. Inspired by Huang et al. [22], we simplify the 3D modeling process by embedding 2D Gaussians within 3D space. We define a local 2D coordinate system using two orthonormal tangent vectors  $t_u$  and  $t_v$ , where each Gaussian point is represented by its center coordinates  $(u, v)$  in this local frame. The 3D position of any point on the 2D Gaussian surface is computed as:

$$P(u, v) = p_k + u \cdot t_u + v \cdot t_v, \quad (2)$$

where  $p_k$  is the center of the Gaussian primitive in world coordinates. Each Gaussian point  $p(u, v)$  is modeled as an elliptical distribution embedded in 3D space, with the mathematical representation:

$$G(p) = \exp\left(-\frac{1}{2}[u, v] \Sigma^{-1} [u, v]^T\right), \quad (3)$$

where  $\Sigma$  is the  $2 \times 2$  covariance matrix controlling the anisotropy and spatial extent of the Gaussian.

To obtain the depth  $z$  for rendering, we employ a wave-splat intersection approach. For an image coordinate  $(x, y)$ , we parameterize the corresponding pixel ray as the intersection of two orthogonal planes: the vertical plane  $X_c \sim x$  with homogeneous representation  $h_x = (-1, 0, 0, x)^T$ , and the horizontal plane  $Y_c \sim y$  with  $h_y = (0, -1, 0, y)^T$ , where  $(X_c, Y_c, z)$  denote the camera coordinate system.

We transform both planes into the local coordinates of the 2D Gaussian primitive using the transformation matrix  $M = WH$ , where  $H$  is the local-to-world transform of the Gaussian surface and  $W$  is the world-to-camera transformation. Following the plane transformation rule, we compute:

$$h_u = (M^{-1})^T h_x, \quad h_v = (M^{-1})^T h_y. \quad (4)$$

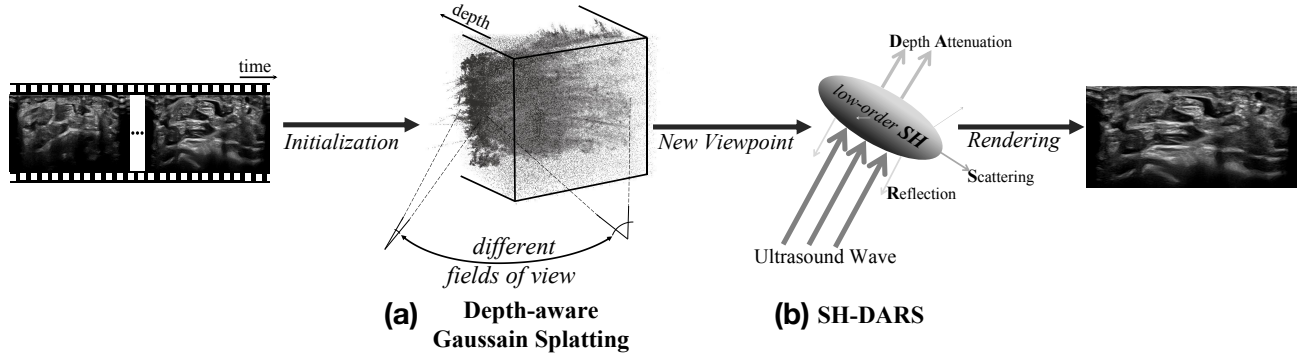


Figure 1. Pipeline of UltraGS. (a) Different Gaussian points are assigned different FoVs to capture more accurate depth information. (Illustrated here is Case 1 from the Clinical Dataset.) In (b), SH-DARS renders new images using novel view information.

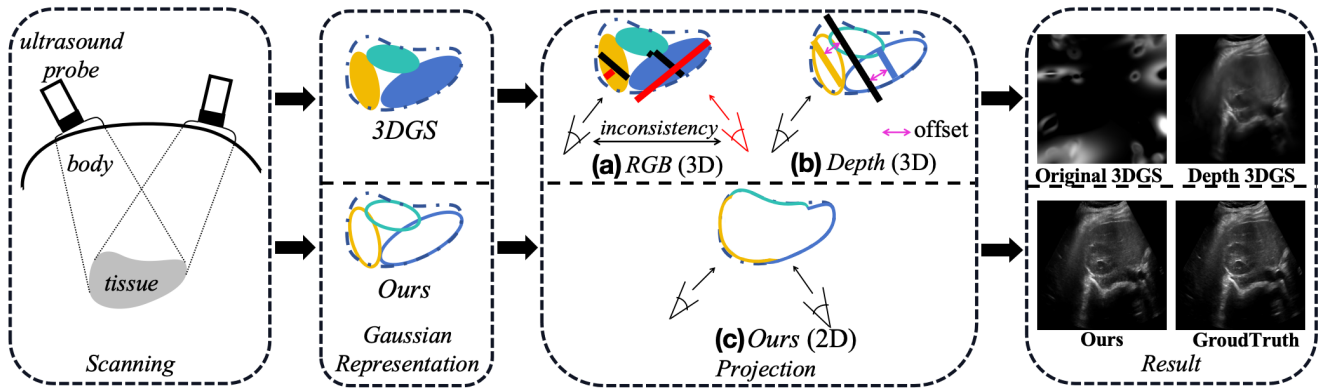


Figure 2. 3DGS uses 3D Gaussian spheres for ultrasound scenes, while UltraGS employs 2D Gaussian disks. In projection, 3DGS faces view inconsistency in RGB (a) and center offset in depth (b), whereas UltraGS’s 2D projection (c) addresses these issues.

The intersection coordinates  $(u, v)$  in the local 2D Gaussian coordinate system are obtained by solving where the transformed ray intersects the Gaussian plane, which can be determined from the projected ray parameters  $h_u$  and  $h_v$ .

Once we have the local intersection coordinates  $(u, v)$ , we compute the 3D world coordinates of this intersection point by evaluating the parametric surface. Converting to homogeneous coordinates:

$$\mathbf{X}_w = \begin{bmatrix} p_k + u \cdot t_u + v \cdot t_v \\ 1 \end{bmatrix}. \quad (5)$$

Finally, the depth  $z$  is obtained by transforming this intersection point to camera coordinates:

$$\mathbf{X}_c = W \cdot \mathbf{X}_w = \begin{bmatrix} X_c \\ Y_c \\ z \\ 1 \end{bmatrix}. \quad (6)$$

This explicit wave-splat intersection ensures perspective-correct depth computation and multi-view consistency, addressing the geometric limitations of traditional 3D Gaussian splatting.

Another key innovation of our approach is the introduction of learnable fields of view to address the unique characteristics of ultrasound imaging.

Unlike traditional RGB cameras with fixed intrinsic parameters, ultrasound imaging presents several fundamental challenges. Points that lie deeper in tissue subtend smaller angles at the transducer than superficial points, requiring the field of view to dynamically adapt with depth to maintain uniform spatial resolution. Additionally, the irregularity of body surfaces during scanning causes substantial variations in the effective FoV, while the absence of traditional camera calibration parameters leads to significant errors when using conventional structure-from-motion methods.

To address these challenges, we introduce learnable FoV parameters  $\theta_x$  and  $\theta_y$  for adaptive projection. The updated fields of view are defined as:

$$FOV_x = 2 \tan^{-1}(e^{\theta_x}), \quad FOV_y = 2 \tan^{-1}(e^{\theta_y}). \quad (7)$$

The world-to-camera transformation matrix  $W$  is a standard  $4 \times 4$  rigid body transformation:

$$W = \begin{bmatrix} R & t \\ 0^T & 1 \end{bmatrix}, \quad (8)$$

where  $R$  is the  $3 \times 3$  rotation matrix and  $t$  is the  $3 \times 1$  translation vector. For the complete 2D–3D correspondence, we follow the standard pinhole camera model:

$$\mathbf{x} \sim K [R|t] \mathbf{X}_w, \quad (9)$$

where  $\mathbf{x} = [x, y, 1]^T$  are homogeneous image coordinates, and  $K$  is the camera intrinsic matrix defined as:

$$K = \begin{bmatrix} f_x & 0 & \frac{W_{\text{img}}}{2} \\ 0 & f_y & \frac{H_{\text{img}}}{2} \\ 0 & 0 & 1 \end{bmatrix}. \quad (10)$$

The focal lengths  $f_x$  and  $f_y$  are related to the learnable fields of view through

$$f_x = \frac{W_{\text{img}}}{2 \tan(\text{FOV}_x/2)}, \quad f_y = \frac{H_{\text{img}}}{2 \tan(\text{FOV}_y/2)},$$

where  $W_{\text{img}}$  and  $H_{\text{img}}$  are the image dimensions.

We leverage COLMAP [32, 33] to obtain the intrinsic parameters of each per-frame camera matrix, which provide initial estimates of  $\text{FOV}_x^{(0)}$  and  $\text{FOV}_y^{(0)}$  and are used to initialize the learnable FoV parameters  $\theta_x$  and  $\theta_y$ . This learnable FoV approach enables accurate 2D projection transformations specifically tailored for ultrasound imaging, where the effective FoV dynamically adjusts to maintain uniform spatial resolution across varying tissue depths while ensuring multi-view projection consistency.

### 3.3. SH-DARS Rendering

In conventional 3DGS, spherical harmonic (SH) functions [13]  $Y_l^m(\theta, \phi)$  are employed to model view-dependent appearance, where  $l$  represents the order of spherical harmonics and  $m$  represents the degree ( $-l \leq m \leq l$ ). The color at a given observation direction  $d = (\theta, \phi)$  is derived as:

$$c(d, k) = \sum_{l=0}^L \sum_{m=-l}^l k_l^m Y_l^m(\theta, \phi) \quad (11)$$

where  $k_l^m$  are learnable coefficients.

While conventional RGB rendering typically uses  $l = 3$  with 16 parameters, ultrasound imaging exhibits fundamentally different characteristics that justify a reduced parameter space. Unlike natural light, ultrasound waves undergo complex interactions including depth-dependent attenuation, specular reflection, and volumetric scattering within tissue. These physical phenomena dominate the appearance variation rather than complex view-dependent effects seen in natural scenes.

Moreover, ultrasound imaging typically exhibits more constrained viewing angles due to the nature of transducer positioning, reducing the complexity of directional variations. Therefore, we adopt  $l = 1$  with 4 parameters for the

base intensity modeling, which provides sufficient representational capacity while enabling real-time performance.

The base intensity  $\mathbf{c}(d, k) = (c_x, c_y, c_z)$  represents the fundamental acoustic response before physical wave interactions. To accurately model ultrasound-specific phenomena, we introduce three physically-motivated components. The depth attenuation follows the Beer-Lambert law [35] for acoustic wave propagation, modeling exponential intensity decay with depth. For computational efficiency, we use the logarithmic approximation commonly employed in ultrasound imaging:

$$I_{\text{att}} = I_0 - \alpha \cdot z, \quad (12)$$

where  $I_0$  is the initial acoustic intensity, and  $\alpha$  is the attenuation coefficient, set to  $\alpha = 1$  in our model. And  $z$  represents the tissue penetration depth.

Accordingly, when the acoustic wave propagates along the  $x$ -axis, the attenuation can be represented as a vector:

$$\mathbf{I}_{\text{att}} = [-\alpha \cdot z, 0, 0]. \quad (13)$$

Acoustic impedance mismatches at tissue boundaries create specular reflections [? ], which we model through a quadratic intensity term that captures the relationship between base intensity and reflection strength:

$$\mathbf{I}_{\text{refl}} = \beta \mathbf{c} \odot \mathbf{c}, \quad (14)$$

where  $\odot$  represents the Hadamard product, and  $\beta$  is a learnable reflection coefficient.

Volumetric scattering from sub-wavelength tissue structures creates diffuse acoustic returns, modeled as cross-channel scattering interactions:

$$\mathbf{I}_{\text{scat}} = (\mathbf{\Gamma} \mathbf{c}) \odot \mathbf{c}, \quad (15)$$

where  $\mathbf{\Gamma} \in \mathbb{R}^{3 \times 3}$  is the learnable scattering coefficient matrix with zero diagonal entries ( $\gamma_{ii} = 0$ ), representing inter-channel coupling.

The final ultrasound intensity is computed by combining these physically-motivated components:

$$\mathbf{I}_{\text{final}} = \mathbf{c}(d, k) + w_{\text{att}} \mathbf{I}_{\text{att}} + w_{\text{refl}} \mathbf{I}_{\text{refl}} + w_{\text{scat}} \mathbf{I}_{\text{scat}} \quad (16)$$

where  $w_{\text{att}}, w_{\text{refl}}, w_{\text{scat}}$  are learnable weight parameters that balance the contribution of each physical effect. This formulation provides a principled approach to modeling ultrasound-specific rendering while maintaining computational efficiency for real-time applications.

## 4. Experiments

### 4.1. Datasets

We evaluate our proposed method on three different ultrasound datasets, each representing distinct imaging scenarios and technical challenges.

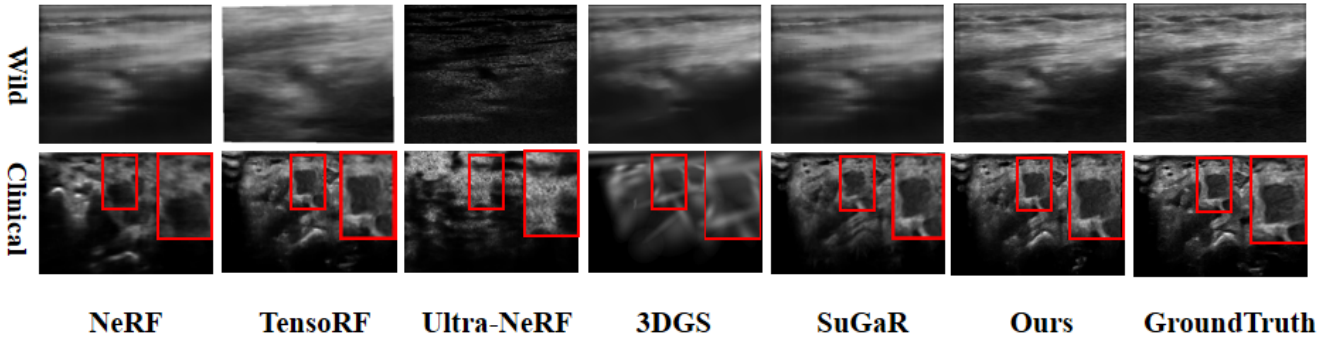


Figure 3. A visual reconstruction comparison on Wild Dataset and Clinical Dataset.

Table 1. Quantitative comparison with other approaches on the Wild Dataset and Phantom Dataset.

Method	Wild Dataset			Phantom Dataset			Speed (fps) $\uparrow$
	PSNR $\uparrow$	SSIM $\uparrow$	MSE $\downarrow$	PSNR $\uparrow$	SSIM $\uparrow$	MSE $\downarrow$	
NeRF	20.176	0.6834	0.0066	20.359	0.6301	0.0058	0.28
TensorRF	24.058	0.7528	0.0051	27.260	0.7178	0.0029	1.61
Ultra-NeRF	19.140	0.6218	0.0109	25.115	0.6814	0.0042	0.43
3DGS	22.327	0.7745	0.0057	27.115	0.7142	0.0031	52.56
SuGaR	21.392	0.6291	0.0159	28.899	0.8843	0.0024	9.81
<b>Ours</b>	<b>25.454</b>	<b>0.7969</b>	<b>0.0043</b>	<b>29.550</b>	<b>0.8966</b>	<b>0.0020</b>	<b>64.69</b>

#### Ultrasound in the Wild Dataset (Wild Dataset) [12]:

This dataset consists of ten knee joint samples acquired using a hand-held Butterfly iQ+ ultrasound device. It primarily focuses on longitudinal suprapatellar recess views, captured through casual sweeps at 30 FPS, with each sweep containing at least 85 frames. Data collection was conducted on healthy subjects under standardized protocols and institutional ethics approval. Due to the uncontrolled clinical environment, multi-view synchronized acquisition was not feasible, which posed significant challenges for camera registration and 3D reconstruction. COLMAP with SfM was employed for pose estimation, and every 8th frame was selected for testing. The handheld acquisition introduces natural motion artifacts and probe trajectory variations, which help assess the robustness of algorithms under realistic imaging conditions.

**Phantom Dataset [36]:** This dataset contains lumbar spine ultrasound scans acquired with a gelatin-based phantom using a robotic manipulator (KUKA LBR iiwa 7 R800) and a linear probe system. It consists of 13 sweeps with 150 frames each, including six pairs of tilted sweeps and one perpendicular sweep, all captured in paramedian sagittal orientation. Nine samples with valid reconstruction information were selected for analysis. The robotic system, integrated with ImFusion, provides precise probe tracking and real-time image acquisition. Variations in probe angles intentionally generate occlusions in the spinous process region, simulating realistic imaging challenges where

anatomical structures block visibility. The controlled phantom environment enables systematic evaluation of reconstruction algorithms under known geometric constraints.

#### Clinical Ultrasound Examination Dataset (Clinical Dataset):

This is our contributed dataset, collected using the Canon i900 ultrasound system with institutional research ethics approval (Ethics Approval No.: \*\*\*\*\*). It consists of six samples: three wrist joint examinations and three kidney scans. Wrist joint cases (1–3) use volar scanning with the probe placed on the palmar surface to visualize carpal tunnel structures, including flexor tendons, the median nerve, and the transverse carpal ligament. The protocol captures both static anatomical features and dynamic probe positioning variations. Kidney cases (4–6) adopt a dual-plane acquisition strategy: transverse scanning from the right flank for cross-sectional visualization, followed by a 90-degree probe rotation for longitudinal sagittal imaging. This multi-planar strategy provides comprehensive organ coverage while introducing probe orientation changes commonly encountered in clinical practice. All examinations follow standardized clinical protocols, ensuring diagnostic relevance while maintaining sufficient image quality for 3D reconstruction evaluation. The dataset will be made publicly available to advance research in clinical ultrasound reconstruction. Importantly, as the data are sourced directly from real clinical examinations, they reflect the inherent complexity of clinical imaging and provide a reliable basis for validating model effectiveness in practical clinical

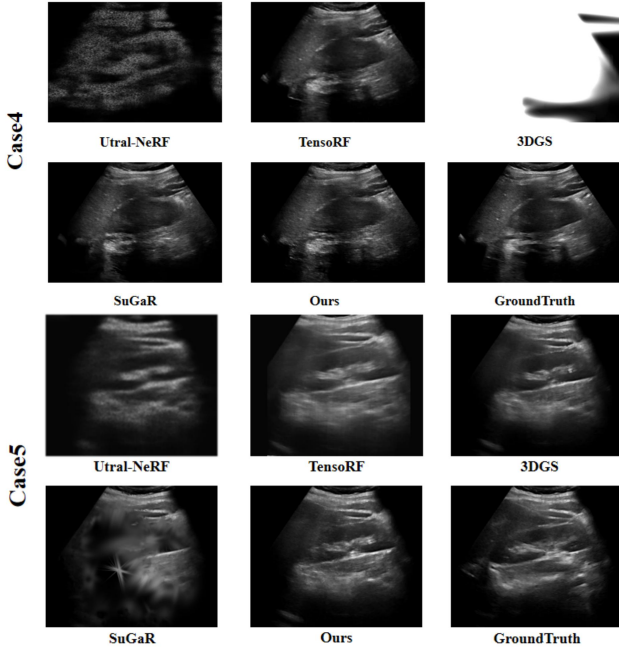


Figure 4. Comparison of kidney sample visualization results from the Clinical Dataset

scenarios.

## 4.2. Experimental Setup

We conducted extensive evaluations of UltraGS for novel view synthesis across three representative ultrasound datasets. For all datasets, the test set was constructed by selecting the last frame from every eight frames, following the protocol in [12, 19, 36]. Performance was evaluated using PSNR, SSIM, and MSE. In addition, we measured inference speed, which is particularly critical for clinical applications. We report the average values of these quantitative metrics across multiple frames. Our proposed method was compared against the following baseline models: NeRF [27], the NeRF-based improvement TensorRF [9], the ultrasound-specific NeRF method Ultra-NeRF [36], 3DGS [24], and the 3DGS-based improvement SuGaR [18]. All experiments were conducted on an Nvidia RTX 3090 GPU.

## 4.3. Quantitative and Qualitative Evaluation

Table 1 presents a quantitative comparison between UltraGS and other methods, on both the Wild and Phantom datasets. Across all evaluation metrics, UltraGS achieves the best performance. Specifically, it consistently obtains the highest PSNR and SSIM values, while simultaneously delivering the lowest MSE, which highlights its superior reconstruction accuracy and image fidelity. Beyond quality, UltraGS also demonstrates exceptional computational efficiency, achieving 64.69 fps, which is more than an order

of magnitude faster than most NeRF-based methods. These results collectively confirm UltraGS’s capability to provide both accurate and efficient novel view synthesis in ultrasound imaging.

Performance on the Clinical Dataset is further summarized in Table 2, where UltraGS consistently outperforms competing methods across all six cases. While NeRF and Ultra-NeRF often suffer from blurred reconstructions with high noise, and 3DGS produces misaligned structures, our method maintains stable improvements in both PSNR and SSIM across diverse patient cases. Even compared with TensorRF and SuGaR, which show partial improvements in specific scenarios, UltraGS achieves more reliable results overall, indicating its strong adaptability to different clinical conditions.

The visual comparisons in Fig. 3 and Fig. 4 provide additional evidence of these advantages. NeRF and Ultra-NeRF reconstructions are heavily degraded by noise and blurring artifacts, while 3DGS reconstructions exhibit noticeable structural misalignments. TensorRF and SuGaR generate sharper details but lack robustness across datasets, leading to inconsistent visual quality. In contrast, UltraGS produces reconstructions that better preserve anatomical boundaries, maintain sharper edge details, and achieve higher contrast, which are closer to the ground truth. This consistency across datasets and clinical cases underscores UltraGS’s effectiveness in capturing complex tissue structures while suppressing noise. More visual results can be found in the **supplementary materials**.

Taken together, both quantitative metrics and qualitative reconstructions demonstrate that UltraGS significantly surpasses existing approaches in terms of accuracy, efficiency, and robustness, making it a strong candidate for clinical ultrasound applications.

## 4.4. Ablation Study

To further investigate the contributions of individual components and the robustness of the model, we conducted ablation studies under two settings: limited training conditions and module removal experiments. The results are reported in Fig.5 and Table 3.

### 4.4.1. Limited Training

We first examined model performance under limited training with only 3,000 iterations and four input views. Under this setting, UltraGS still maintained clear structural reconstructions and faster convergence compared to TensorRF and 3DGS. Specifically, while TensorRF reconstructions remained blurry and failed to capture fine anatomical boundaries, 3DGS suffered from distortions and missing details. In contrast, UltraGS produced reconstructions with sharper tissue boundaries and more accurate anatomical structures, closely resembling the ground truth. This

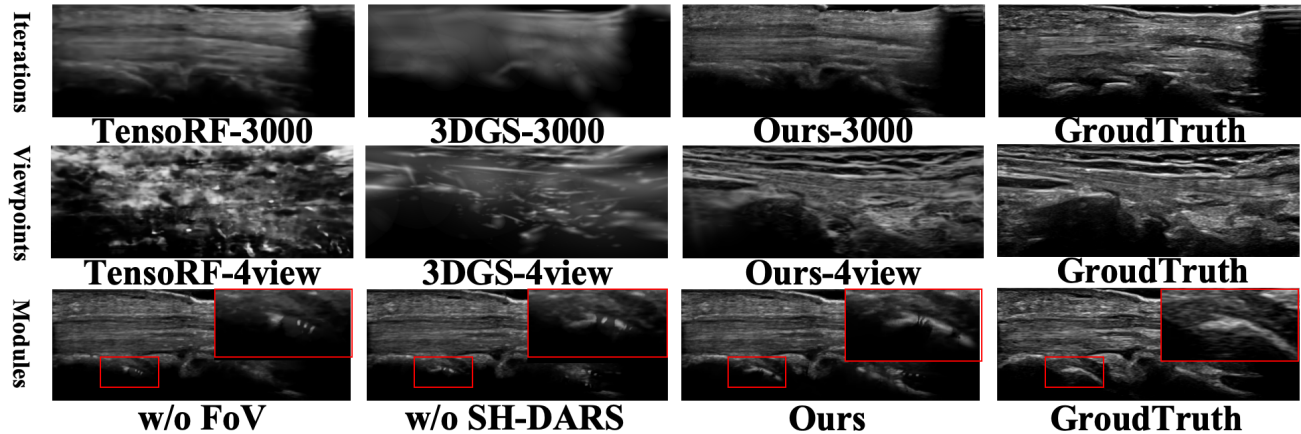


Figure 5. Ablation study of iteration number, viewpoints, and modules of learnable FoV/SH-DARS.

Table 2. Quantitative comparison with other approaches in Clinical Dataset.

Method	Case1		Case2		Case3		Case4		Case5		Case6	
	PSNR	SSIM										
NeRF	18.282	0.3388	21.880	0.5363	17.329	0.3835	23.119	0.5985	21.634	0.5980	25.376	0.6660
TensoRF	17.206	0.3593	22.787	0.6378	19.999	0.5124	22.681	0.5692	22.252	0.6816	26.158	0.7389
Ultra-NeRF	17.661	0.2404	18.194	0.3994	19.030	0.3335	19.053	0.4331	20.648	0.4971	22.450	0.7030
3DGS	17.280	0.4270	20.367	0.5510	18.524	0.4420	21.807	0.6673	22.110	0.6773	25.927	0.7333
SuGaR	18.170	0.4601	23.831	0.7085	20.902	0.5128	23.541	0.6381	20.135	0.5923	27.264	0.7721
<b>Ours</b>	<b>18.846</b>	<b>0.4978</b>	<b>24.644</b>	<b>0.7380</b>	<b>21.570</b>	<b>0.5493</b>	<b>24.030</b>	<b>0.6719</b>	<b>22.723</b>	<b>0.6911</b>	<b>28.181</b>	<b>0.7888</b>

experiment demonstrates the model’s ability to learn efficiently from limited data, which is particularly valuable in medical imaging where training resources can be constrained.

#### 4.4.2. Module Removal

We further evaluated the importance of the two key components of UltraGS: the learnable FoV and SH-DARS. As shown in Table 3, removing either module resulted in noticeable performance degradation across both datasets. Without learnable FoVs, the model failed to correctly capture geometric properties such as depth and size, leading to structure loss and dark artifacts in the reconstructions. When SH-DARS was removed, the results suffered from intensity inconsistencies and reduced overall image quality. By contrast, the full UltraGS model achieved the best performance in all metrics, confirming that both components are crucial for robust reconstruction and faithful rendering.

Together, the ablation studies highlight that UltraGS is not only efficient under constrained training but also relies on the synergy of its novel components to achieve great performance in ultrasound novel view synthesis.

Table 3. Ablation Study on Module Removal.

Variant	Wild Dataset		Phantom Dataset	
	PSNR	SSIM	PSNR	SSIM
w/o Learnable FoVs	23.422	0.7520	27.105	0.8500
w/o SH-DARS	23.887	0.7610	27.451	0.8320
<b>Ours (Full model)</b>	<b>25.454</b>	<b>0.7969</b>	<b>29.550</b>	<b>0.8966</b>

## 5. Conclusion

This study is the first to apply Gaussian splatting to novel view synthesis in ultrasound imaging, filling a gap in this research field. By developing a depth-aware Gaussian splatting method, we achieved accurate 3D structural reconstruction of ultrasound data. Subsequently, the SH-DARS rendering, which integrates a low-order spherical harmonic function with ultrasound wave properties, effectively represents structural intensity. Our method demonstrated superior performance in novel view generation across wild, phantom, and clinical datasets, achieving state-of-the-art results while maintaining the fastest processing speed. This highlights its robustness and efficiency, making it a promising solution for the ultrasound clinical application of AI models.

## References

- [1] Chrissy A Adriaans, Mark Wijkhuizen, Lennard M van Karnebeek, Freija Geldof, and Behdad Dashtbozorg. Trackerless 3d freehand ultrasound reconstruction: A review. *Applied Sciences*, 14(17):7991, 2024.
- [2] Ricardo Scott Avila, Lisa Sobierajski Avila, Brian Peter Geiser, William Thomas Hatfield, and Todd Michael Tillman. Method and apparatus for displaying 3d ultrasound data using three modes of operation, 1999. US Patent 5,934,288.
- [3] Yanqi Bao, Tianyu Ding, Jing Huo, Yaoli Liu, Yuxin Li, Wenbin Li, Yang Gao, and Jiebo Luo. 3d gaussian splatting: Survey, technologies, challenges, and opportunities. *IEEE Transactions on Circuits and Systems for Video Technology*, 2025.
- [4] Jonathan T Barron, Ben Mildenhall, Matthew Tancik, Peter Hedman, Ricardo Martin-Brualla, and Pratul P Srinivasan. Mip-nerf: A multiscale representation for anti-aliasing neural radiance fields. In *Proceedings of the IEEE/CVF international conference on computer vision*, pages 5855–5864, 2021.
- [5] Jonathan T Barron, Ben Mildenhall, Dor Verbin, Pratul P Srinivasan, and Peter Hedman. Mip-nerf 360: Unbounded anti-aliased neural radiance fields. In *Proceedings of the IEEE/CVF conference on computer vision and pattern recognition*, pages 5470–5479, 2022.
- [6] Brian Cabral, Marc Olano, and Philip Nemecek. Reflection space image based rendering. In *Proceedings of the 26th annual conference on Computer graphics and interactive techniques*, pages 165–170, 1999.
- [7] Yuanhao Cai, Yixun Liang, Jiahao Wang, Angtian Wang, Yulun Zhang, Xiaokang Yang, Zongwei Zhou, and Alan Yuille. Radiative gaussian splatting for efficient x-ray novel view synthesis. In *European Conference on Computer Vision*, pages 283–299. Springer, 2024.
- [8] Vincent Chan and Anahi Perlas. Basics of ultrasound imaging. In *Atlas of ultrasound-guided procedures in interventional pain management*, pages 13–19. Springer, 2010.
- [9] Anpei Chen, Zexiang Xu, Andreas Geiger, Jingyi Yu, and Hao Su. Tensorf: Tensorial radiance fields. In *European conference on computer vision*, pages 333–350. Springer, 2022.
- [10] Xin Chen, Houjin Chen, Yahui Peng, Liu Liu, and Chang Huang. A freehand 3d ultrasound reconstruction method based on deep learning. *Electronics*, 12(7):1527, 2023.
- [11] Zhiqin Chen, Thomas Funkhouser, Peter Hedman, and Andrea Tagliasacchi. Mobilenerf: Exploiting the polygon rasterization pipeline for efficient neural field rendering on mobile architectures. In *Proceedings of the IEEE/CVF Conference on Computer Vision and Pattern Recognition*, pages 16569–16578, 2023.
- [12] Rishit Dagli, Atsuhiko Hibi, Rahul G Krishnan, and Pascal N Tyrrell. Nerf-us: Removing ultrasound imaging artifacts from neural radiance fields in the wild. *arXiv preprint arXiv:2408.10258*, 2024.
- [13] Sara Fridovich-Keil, Alex Yu, Matthew Tancik, Qinhong Chen, Benjamin Recht, and Angjoo Kanazawa. Plenoxels: Radiance fields without neural networks. In *Proceedings of the IEEE/CVF conference on computer vision and pattern recognition*, pages 5501–5510, 2022.
- [14] Zhongpai Gao, Benjamin Planche, Meng Zheng, Xiao Chen, Terrence Chen, and Ziyang Wu. Ddgs-ct: Direction-disentangled gaussian splatting for realistic volume rendering. In *Advances in Neural Information Processing Systems*, pages 39281–39302. Curran Associates, Inc., 2024.
- [15] Zhongpai Gao, Benjamin Planche, Meng Zheng, Xiao Chen, Terrence Chen, and Ziyang Wu. Ddgs-ct: Direction-disentangled gaussian splatting for realistic volume rendering. In *The Thirty-eighth Annual Conference on Neural Information Processing Systems*, 2024.
- [16] Assaf Govari. Three-dimensional reconstruction using ultrasound, 2004. US Patent 6,716,166.
- [17] Hao Guan and Mingxia Liu. Domain adaptation for medical image analysis: a survey. *IEEE Transactions on Biomedical Engineering*, 69(3):1173–1185, 2021.
- [18] Antoine Guédon and Vincent Lepetit. Sugar: Surface-aligned gaussian splatting for efficient 3d mesh reconstruction and high-quality mesh rendering. In *Proceedings of the IEEE/CVF Conference on Computer Vision and Pattern Recognition*, pages 5354–5363, 2024.
- [19] Ziwen Guo, Zi Fang, and Zhuang Fu. Ulre-nerf: 3d ultrasound imaging through neural rendering with ultrasound reflection direction parameterization. *arXiv preprint arXiv:2408.00860*, 2024.
- [20] R James Housden, Andrew H Gee, Graham M Treece, and Richard W Prager. Sensorless reconstruction of unconstrained freehand 3d ultrasound data. *Ultrasound in medicine & biology*, 33(3):408–419, 2007.
- [21] Wenbo Hu, Yuling Wang, Lin Ma, Bangbang Yang, Lin Gao, Xiao Liu, and Yuewen Ma. Tri-miprf: Tri-mip representation for efficient anti-aliasing neural radiance fields. In *Proceedings of the IEEE/CVF International Conference on Computer Vision*, pages 19774–19783, 2023.
- [22] Binbin Huang, Zehao Yu, Anpei Chen, Andreas Geiger, and Shenghua Gao. 2d gaussian splatting for geometrically accurate radiance fields. In *ACM SIGGRAPH 2024 conference papers*, pages 1–11, 2024.
- [23] Georgios A Kaissis, Marcus R Makowski, Daniel Rückert, and Rickmer F Braren. Secure, privacy-preserving and federated machine learning in medical imaging. *Nature Machine Intelligence*, 2(6):305–311, 2020.
- [24] Bernhard Kerbl, Georgios Kopanas, Thomas Leimkühler, and George Drettakis. 3d gaussian splatting for real-time radiance field rendering. *ACM Trans. Graph.*, 42(4):139–1, 2023.
- [25] Raja Kumar and Vanshika Vats. Few-shot novel view synthesis using depth aware 3d gaussian splatting. In *European Conference on Computer Vision*, pages 1–13. Springer, 2024.
- [26] Mingyuan Luo, Xin Yang, Hongzhang Wang, Liwei Du, and Dong Ni. Deep motion network for freehand 3d ultrasound reconstruction. In *International Conference on Medical Image Computing and Computer-Assisted Intervention*, pages 290–299. Springer, 2022.
- [27] Ben Mildenhall, Pratul P Srinivasan, Matthew Tancik, Jonathan T Barron, Ravi Ramamoorthi, and Ren Ng. Nerf:

- Representing scenes as neural radiance fields for view synthesis. *Communications of the ACM*, 65(1):99–106, 2021.
- [28] Amirali Molaei, Amirhossein Aminimehr, Armin Tavakoli, Amirhossein Kazerouni, Bobby Azad, Reza Azad, and Dorit Merhof. Implicit neural representation in medical imaging: A comparative survey. In *Proceedings of the IEEE/CVF International Conference on Computer Vision*, pages 2381–2391, 2023.
- [29] Mohammad Hamed Mozaffari and Won-Sook Lee. Freehand 3-d ultrasound imaging: a systematic review. *Ultrasound in medicine & biology*, 43(10):2099–2124, 2017.
- [30] Christian Reiser, Songyou Peng, Yiyi Liao, and Andreas Geiger. Kilonerf: Speeding up neural radiance fields with thousands of tiny mlps. In *Proceedings of the IEEE/CVF international conference on computer vision*, pages 14335–14345, 2021.
- [31] Christian Reiser, Rick Szeliski, Dor Verbin, Pratul Srinivasan, Ben Mildenhall, Andreas Geiger, Jon Barron, and Peter Hedman. Merf: Memory-efficient radiance fields for real-time view synthesis in unbounded scenes. *ACM Transactions on Graphics (TOG)*, 42(4):1–12, 2023.
- [32] Johannes Lutz Schönberger and Jan-Michael Frahm. Structure-from-motion revisited. In *Conference on Computer Vision and Pattern Recognition (CVPR)*, 2016.
- [33] Johannes Lutz Schönberger, Enliang Zheng, Marc Pollefeys, and Jan-Michael Frahm. Pixelwise view selection for unstructured multi-view stereo. In *European Conference on Computer Vision (ECCV)*, 2016.
- [34] Ole Vegard Solberg, Frank Lindseth, Hans Torp, Richard E Blake, and Toril A Nagelhus Hernes. Freehand 3d ultrasound reconstruction algorithms—a review. *Ultrasound in medicine & biology*, 33(7):991–1009, 2007.
- [35] Donald F Swinehart. The beer-lambert law. *Journal of chemical education*, 39(7):333, 1962.
- [36] Magdalena Wysocki, Mohammad Farid Azampour, Christine Eilers, Benjamin Busam, Mehrdad Salehi, and Nassir Navab. Ultra-nerf: Neural radiance fields for ultrasound imaging. In *Medical Imaging with Deep Learning*, pages 382–401. PMLR, 2024.
- [37] Yuezhe Yang, Yonglin Chen, Xingbo Dong, Junning Zhang, Chihui Long, Zhe Jin, and Yong Dai. An annotated heterogeneous ultrasound database. *Scientific Data*, 12(1):148, 2025.
- [38] Yuezhe Yang, Boyu Yang, Yaqian Wang, Yang He, Xingbo Dong, and Zhe Jin. Explicit and implicit representations in ai-based 3d reconstruction for radiology: A systematic literature review. *arXiv preprint arXiv:2504.11349*, 2025.
- [39] Alex Yu, Ruilong Li, Matthew Tancik, Hao Li, Ren Ng, and Angjoo Kanazawa. Plenotrees for real-time rendering of neural radiance fields. In *Proceedings of the IEEE/CVF international conference on computer vision*, pages 5752–5761, 2021.
- [40] Zehao Yu, Anpei Chen, Binbin Huang, Torsten Sattler, and Andreas Geiger. Mip-splatting: Alias-free 3d gaussian splatting. In *Proceedings of the IEEE/CVF conference on computer vision and pattern recognition*, pages 19447–19456, 2024.
- [41] Zhechen Yuan, Binzhe Yuan, Chaolin Rao, Yiren Zhu, Yunxiang He, Pingqiang Zhou, Jingyi Yu, and Xin Lou. A neural rendering coprocessor with optimized ray representation and marching. *IEEE Transactions on Very Large Scale Integration (VLSI) Systems*, 2025.
- [42] Matthias Zwicker, Hanspeter Pfister, Jeroen Van Baar, and Markus Gross. Ewa volume splatting. In *Proceedings Visualization, 2001. VIS'01.*, pages 29–538. IEEE, 2001.
- [43] Matthias Zwicker, Hanspeter Pfister, Jeroen Van Baar, and Markus Gross. Surface splatting. In *Proceedings of the 28th annual conference on Computer graphics and interactive techniques*, pages 371–378, 2001.

## A. Research Motivation

### A.1. FoV Variations Within a Single Ultrasound Scan

Ultrasound imaging has established itself as an indispensable clinical diagnostic tool due to its non-invasive nature, real-time capabilities, and cost-effectiveness. However, unlike conventional optical imaging systems with relatively fixed fields of view (FoV), ultrasound imaging inherently exhibits a field of view that varies within a single scan. These intra-scan FoV variations significantly affect the quality of three-dimensional reconstructions and, consequently, the accuracy of clinical diagnoses and treatment planning.

In clinical practice, physicians typically perform ultrasound scans by manually manipulating a probe across the patient’s body surface. This process introduces several sources of FoV variability during a single scan:

- **Body Surface Irregularities:** The irregular geometry of the human body changes the incident angle of the probe during scanning, leading to spatially and temporally varying FoV coverage and making traditional camera calibration methods difficult to apply.
- **Tissue Depth Effects:** With increasing depth, the effective angular coverage at the probe for deeper tissues commonly becomes narrower, producing non-uniform spatial resolution along depth and requiring corrections that account for intra-scan FoV changes.
- **View-dependent Consistency Issues:** The anisotropic propagation and reflection properties of ultrasound waves cause the apparent FoV to change with probe orientation and position during a single scan, creating inconsistencies that hinder robust multi-view fusion and novel view synthesis.

Conventional approaches such as wobbling probes and 2D probe arrays partially mitigate these issues but remain heavily dependent on manual alignment, introduce potential errors, and involve prohibitive costs that limit their widespread clinical adoption.

### A.2. Advancements and Limitations in 3DGS

In 2023, 3D Gaussian Splatting (3DGS) [24] emerged as a solution to address NeRF’s computational constraints. By employing explicit Gaussian primitives, 3DGS achieves real-time rendering while preserving fine details and accommodating viewpoint changes. In the medical imaging domain, 3DGS has already provided new solutions for CT reconstruction from X-ray images.

Nevertheless, fundamental differences between B-mode ultrasound, natural light, and X-ray imaging present significant challenges when applying 3DGS directly to ultrasound:

- **Inadequate Depth Information Processing:** In ultrasound imaging, depth information is crucial for interpreting tissue structures, yet this factor is frequently overlooked in 3DGS methods developed for natural images.
- **Absence of Wave Propagation Characteristics:** Ultrasound imaging involves not only simple anisotropy (which can be addressed through spherical harmonics) but also complex wave propagation phenomena including attenuation, reflection, and scattering, which must be explicitly modeled to achieve realistic rendering.

Addressing the aforementioned challenges, we present UltraGS, a real-time ultrasound-aware 3D Gaussian splatting framework specifically tailored for B-mode imaging.

## B. Why COLMAP for Ultrasound Imaging

### B.1. Effectiveness of COLMAP

COLMAP [32, 33], as a structure-from-motion (SfM) approach, offers a viable solution for the initial registration of ultrasound images without requiring specialized hardware. The effectiveness of COLMAP for initial pose estimation in our ultrasound imaging context stems from its hardware independence, enabling pose estimation using only image data and eliminating the need for external tracking devices or specialized probes. This makes the technology more accessible for widespread clinical adoption. Through feature-based matching across multiple ultrasound frames, COLMAP establishes geometric relationships between different views, providing initial estimates of camera positions. Its bundle adjustment process iteratively refines camera parameters and 3D point positions, helping to mitigate accumulation errors and improve the global consistency of the reconstructed scene. Furthermore, COLMAP offers a largely automated workflow that can process batches of ultrasound images with minimal user intervention, streamlining the initial registration process. These capabilities make COLMAP a practical starting point for establishing spatial relationships between ultrasound images, particularly in the absence of external tracking systems.

## B.2. Limitations of COLMAP

Despite its utility for initial registration, direct application of COLMAP to ultrasound imaging presents significant limitations that necessitate further refinement. Ultrasound images typically exhibit lower contrast and fewer distinctive features compared to natural images, resulting in sparse feature matching that compromises the robustness of COLMAP’s pose estimation. The appearance of anatomical structures in ultrasound varies dramatically with viewing angle due to the physics of acoustic wave propagation, violating COLMAP’s assumption of viewpoint consistency for feature matching. Additionally, ultrasound imaging produces depth-dependent artifacts and shadowing effects that can mislead COLMAP’s structure-from-motion algorithms, resulting in distorted spatial reconstructions. Without metric calibration, COLMAP reconstructions suffer from scale ambiguity, which is particularly problematic in medical applications where accurate measurements are essential for diagnosis and treatment planning. The cumulative effect of these issues leads to registration errors that, while acceptable as initialization, are inadequate for high-precision medical applications without further refinement. These limitations underscore why direct COLMAP registration, while valuable as an initialization step, requires substantial adaptation and enhancement for reliable ultrasound image registration.

## B.3. Alternative Approach: UltraNeRF

In UltraNeRF [36], pose information is accurately derived from a robotic arm, providing precise spatial tracking for 3D ultrasound reconstruction. This approach offers several advantages in terms of technical performance. Robotic arms can achieve sub-millimeter positional accuracy and fraction-of-degree rotational precision, far exceeding what is possible with vision-based methods like COLMAP. Continuous tracking eliminates temporal gaps in pose estimation, ensuring smooth trajectories and consistent spatial relationships between sequential frames. These systems provide absolute metric measurements without scale ambiguity, critical for clinical applications requiring accurate dimensional assessment. Furthermore, pose estimation remains reliable regardless of ultrasound image quality, contrast, or the presence of artifacts.

Despite these substantial benefits, we deliberately chose not to adopt a robotic arm-based approach for several compelling clinical considerations. Robotic systems significantly disrupt established clinical workflows, requiring specialized training and potentially extending examination times, which conflicts with the efficiency demands of busy clinical settings. Precision robotic arms represent substantial capital investments (often exceeding \$50,000) that are prohibitive for many healthcare facilities, particularly in resource-constrained environments. The setup, calibration, and maintenance of robotic systems introduce additional technical complexity that may not be feasible in routine clinical practice. From a patient perspective, robotic arms can be intimidating and potentially limit the sonographer’s ability to adapt to patient movement or discomfort during examination. Perhaps most significantly, the integration of robotic arms compromises the portability of ultrasound systems, one of their key advantages in emergency medicine, point-of-care applications, and remote settings. Our decision to forgo robotic registration aligns with our objective to develop solutions that can be readily integrated into existing clinical ultrasound practices without imposing prohibitive costs or workflow disruptions.

## B.4. Why UltraNeRF Fails

When we applied UltraNeRF with COLMAP-derived poses instead of robotic arm tracking, we observed significantly degraded performance. This degradation can be attributed to several interconnected factors. UltraNeRF was designed and optimized under the assumption of highly accurate pose information from robotic tracking. The relatively larger errors in COLMAP-derived poses propagate through the network, substantially reducing reconstruction quality. The architecture lacks mechanisms to compensate for pose inaccuracies, resulting in cumulative errors that manifest as blurring, ghosting, and geometric distortions in the reconstructed volumes.

COLMAP’s challenges with depth estimation in ultrasound images create inconsistent spatial relationships that compromise UltraNeRF’s ability to model coherent 3D structures. UltraNeRF’s rendering approach does not adequately account for the strong view-dependent characteristics of ultrasound when trained with imprecise pose information, leading to artifacts when synthesizing novel views. The combination of noisy pose estimates and UltraNeRF’s optimization strategy often results in convergence to suboptimal solutions or even optimization failure in severe cases. These findings highlight a fundamental limitation: methods like UltraNeRF that are developed and optimized for high-precision robotic pose information cannot be directly adapted to scenarios with less accurate pose estimation without substantial architectural modifications.

## B.5. Our Approach

Our analysis demonstrates that while COLMAP provides a valuable initialization for ultrasound image registration, its direct application is insufficient for high-quality 3D reconstruction. Similarly, while robotic tracking offers superior precision, its

clinical implementation barriers are substantial. This motivates our introduction of learnable FoV parameters within the UltraGS framework, which fundamentally addresses the registration limitations inherent in ultrasound imaging.

The learnable FoV approach dynamically adapts to the unique characteristics of ultrasound data acquisition, where viewing angles vary substantially due to probe manipulation and tissue interfaces. By allowing each Gaussian primitive to optimize its own field-of-view parameters during training, our method effectively compensates for the registration inaccuracies introduced by COLMAP. This adaptability is particularly crucial in ultrasound imaging, where the angular coverage of acoustic waves changes with tissue depth and composition.

Furthermore, the learnable FoV parameters enable our model to account for the anisotropic nature of ultrasound data without requiring perfect initial registration. As the model trains, these parameters adjust to capture the correct spatial relationships between anatomical structures across different views, effectively refining the initial COLMAP poses without explicit pose optimization. This approach preserves the clinical workflow advantages of hardware-independent imaging while achieving reconstruction quality comparable to systems with specialized tracking hardware.

## C. Mathematical Definitions and Formulations

This section elaborates on the core mathematical formulations of UltraGS approach, focusing on the geometric representation and projection.

### C.1. Geometric Parameterization of a 2D Gaussian

The fundamental primitive in our model is an oriented 2D Gaussian disk, intrinsically representing a local surface element. Its geometry is parameterized by:

- **Center Position:**  $\mathbf{p}_k \in \mathbb{R}^3$  defines the world coordinates of the disk’s center.
- **Tangent Vectors:** Two orthonormal vectors  $\mathbf{t}_u, \mathbf{t}_v \in \mathbb{R}^3$  span the local tangent plane of the disk.
- **Scaling Factors:**  $s_u, s_v \in \mathbb{R}^+$  control the anisotropic spread (variance) of the Gaussian along  $\mathbf{t}_u$  and  $\mathbf{t}_v$ .

The surface normal vector, crucial for defining the disk’s orientation in 3D space, is derived as:

$$\mathbf{n} = \mathbf{t}_w = \mathbf{t}_u \times \mathbf{t}_v \quad (17)$$

The set  $\{\mathbf{t}_u, \mathbf{t}_v, \mathbf{t}_w\}$  forms an orthonormal basis, fully defining the local coordinate frame of the Gaussian.

Any point on the surface of this 2D Gaussian disk can be expressed in the local  $(u, v)$  coordinate system as:

$$\mathbf{P}(u, v) = \mathbf{p}_k + s_u \mathbf{t}_u u + s_v \mathbf{t}_v v \quad (18)$$

This parametric form defines a planar surface in  $\mathbb{R}^3$ .

### C.2. Homogeneous Transformation

To facilitate projective transformations, we represent the geometry of the 2D Gaussian using a homogeneous transformation matrix  $\mathbf{H} \in \mathbb{R}^{4 \times 4}$ :

$$\mathbf{H} = \begin{bmatrix} s_u \mathbf{t}_u & s_v \mathbf{t}_v & \mathbf{0} & \mathbf{p}_k \\ 0 & 0 & 0 & 1 \end{bmatrix} = \begin{bmatrix} \mathbf{RS} & \mathbf{p}_k \\ \mathbf{0}^T & 1 \end{bmatrix} \quad (19)$$

where  $\mathbf{R} = [\mathbf{t}_u, \mathbf{t}_v, \mathbf{t}_w]$  is the rotation matrix and  $\mathbf{S} = \text{diag}(s_u, s_v, 0)$  is the scaling matrix. A point in local homogeneous coordinates  $\mathbf{u} = (u, v, 1, 1)^T$  is transformed to world coordinates by  $\mathbf{X}_w = \mathbf{H}\mathbf{u}$ .

### C.3. Perspective-Accurate Projection via Wave-Splat Intersection

A key advantage of the 2D Gaussian basis lies in its perspective-accurate projection, which is achieved by explicitly solving the wave-splat intersection, thereby overcoming the limitations of the affine approximation in 3DGS.

For a pixel with image coordinates  $\mathbf{x} = (x, y)$ , the corresponding camera ray is defined as the intersection of two planes:  $x$ -plane:  $\mathbf{h}_x = (-1, 0, 0, x)^T$ , and  $y$ -plane:  $\mathbf{h}_y = (0, -1, 0, y)^T$ .

These planes are transformed into the local coordinate system of the Gaussian splat using the inverse transpose of the combined transformation  $\mathbf{M} = \mathbf{WH}$ :

$$\mathbf{h}_u = (\mathbf{WH})^{-\top} \mathbf{h}_x \approx (\mathbf{WH})^\top \mathbf{h}_x, \quad \mathbf{h}_v = (\mathbf{WH})^{-\top} \mathbf{h}_y \approx (\mathbf{WH})^\top \mathbf{h}_y \quad (20)$$

The approximation avoids explicit matrix inversion, enhancing numerical stability.

The intersection point  $(u^*, v^*)$  between the ray and the Gaussian plane is found by solving:

$$\mathbf{h}_u \cdot (u, v, 1, 1)^T = 0, \quad \mathbf{h}_v \cdot (u, v, 1, 1)^T = 0 \quad (21)$$

This yields the solution:

$$u^* = \frac{\mathbf{h}_v^2 \mathbf{h}_u^4 - \mathbf{h}_u^2 \mathbf{h}_v^4}{\mathbf{h}_u^1 \mathbf{h}_v^2 - \mathbf{h}_u^2 \mathbf{h}_v^1}, \quad v^* = \frac{\mathbf{h}_u^1 \mathbf{h}_v^4 - \mathbf{h}_v^1 \mathbf{h}_u^4}{\mathbf{h}_u^1 \mathbf{h}_v^2 - \mathbf{h}_u^2 \mathbf{h}_v^1} \quad (22)$$

where  $\mathbf{h}_u^i$  denotes the  $i$ -th component of the 4D vector  $\mathbf{h}_u$ .

The **depth**  $z$  of the intersection point is obtained by projecting the corresponding 3D point  $\mathbf{P}(u^*, v^*)$  back into camera coordinates using  $\mathbf{W}$  and extracting the  $z$ -component.

## D. Visualization Results

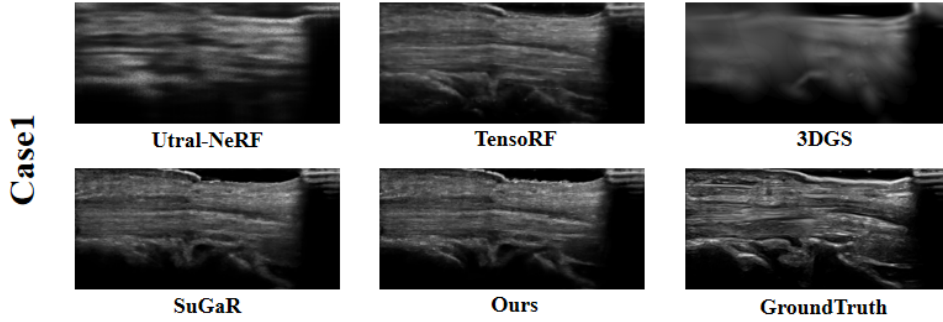


Figure 6. Visual Comparison for Case 1 in the Clinical Dataset.

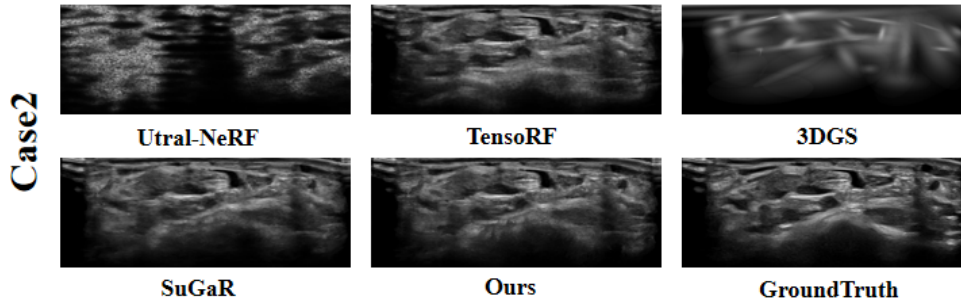


Figure 7. Visual Comparison for Case 2 in the Clinical Dataset.

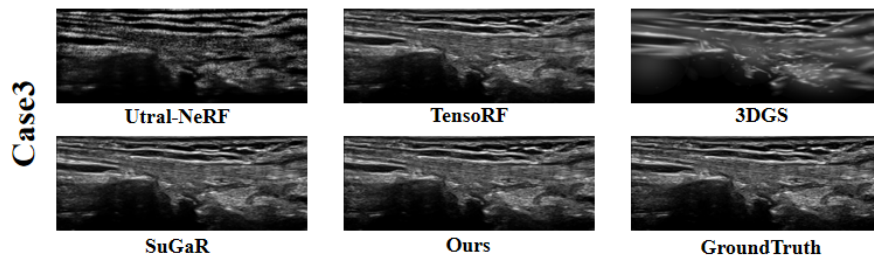


Figure 8. Visual Comparison fo Case 3 in the Clinical Dataset.

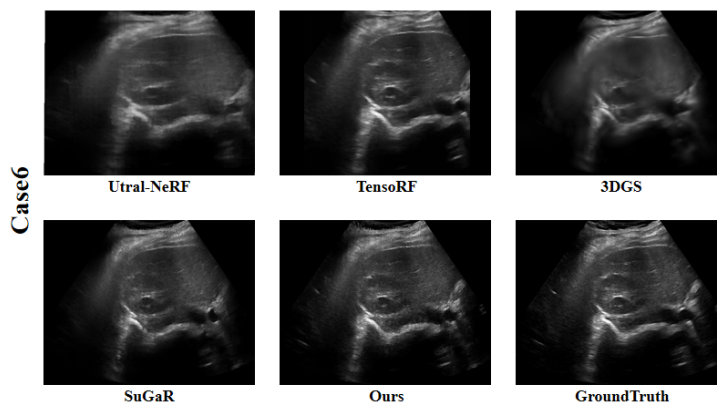


Figure 9. Visual Comparison fo Case 6 in the Clinical Dataset.

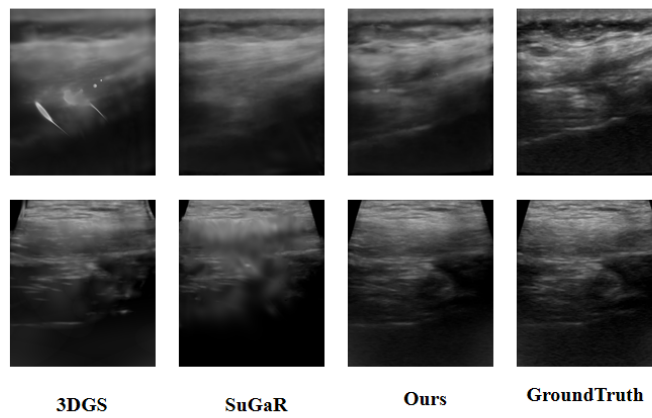


Figure 10. Visual Comparison for Wild Dataset.

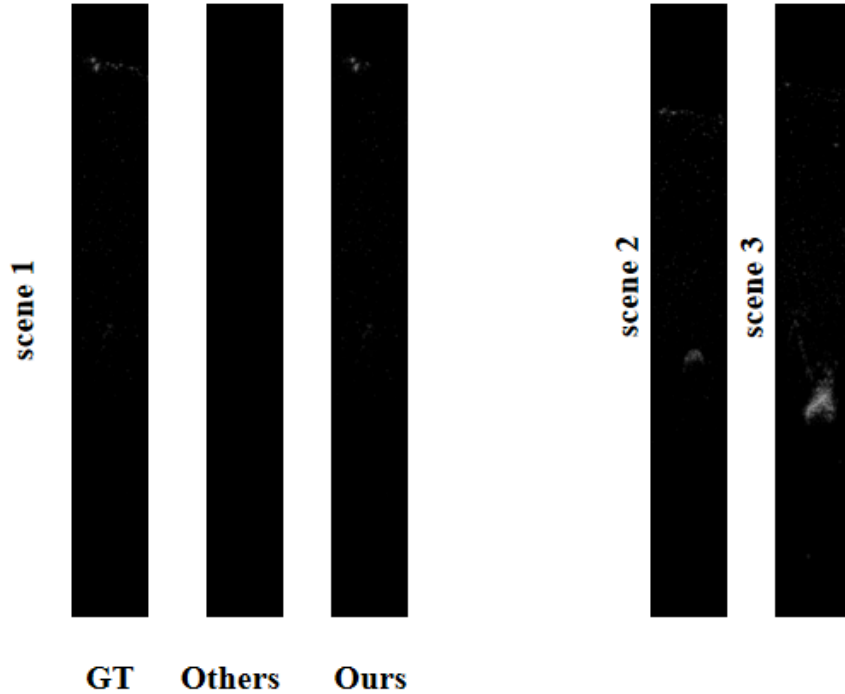


Figure 11. Visual Comparison for Phantom Dataset.

From the supplementary experimental results of Fig.6-9 on the Clinical Dataset, UltraGS showed significant advantages in multiple typical cases (Case 1 to Case 6). Compared with other methods [9, 18, 24, 27, 36], UltraGS has achieved better results in the restoration of boundary details, preservation of tissue structure, and clarity of overall reconstruction, demonstrating its robustness and generalization ability in processing complex clinical data. These results fully validate the adaptability of our method in real clinical environments, especially in the face of poor image quality or blurry structural features, UltraGS can still accurately capture key structural information and achieve stable and high-quality novel view synthesis.

Fig.10 and Fig.11 further expand the evaluation of UltraGS on other datasets (Wild Dataset and Phantom Dataset), with comparison methods including existing Gaussian Splatting based advanced methods such as 3DGS and SuGaR [18, 24]. As shown in Figure 7, on the more challenging Wild Dataset, UltraGS avoids the blurring phenomenon that SuGaR may experience in certain areas while maintaining reconstruction integrity, and outperforms 3DGS in detail restoration.

Fig. 11 presents a visual comparison on the Phantom Dataset, featuring a reconstruction results chart of various methods on the left. The dataset demonstration on the right illustrates its structural characteristics and inherent limitations.

## E. Limitations

Although UltraGS advances real-time ultrasound rendering by modeling depth and acoustic propagation, several limitations remain for its adoption in precise clinical workflows. Firstly, the model abstracts complex tissue heterogeneity and non-linear wave propagation using simplified physical priors, which may limit its fidelity in anatomically diverse or pathological regions. Secondly, while UltraGS introduces learnable FoVs to compensate for unknown or inconsistent probe calibration, this data-driven adjustment remains a surrogate solution. A more principled and clinically robust approach would involve developing an ultrasound-specific version of COLMAP. Finally, although UltraGS shows strong quantitative performance, its clinical trustworthiness and diagnostic value must be further validated through physician-in-the-loop studies.